Dynamic Imaging of the Eye, Optic Nerve, and Extraocular Muscles With Golden Angle Radial MRI

Saikat Sengupta,[1,2] David S. Smith,[1,2] Alex K. Smith,[3] E. Brian Welch,[1,2,4] and Seth A. Smith[1,2,4]

[1]Vanderbilt University Institute of Imaging Science, Vanderbilt University Medical Center, Nashville, Tennessee, United States
[2]Department of Radiology and Radiological Sciences, Vanderbilt University Medical Center, Nashville, Tennessee, United States
[3]The Centre for Functional MRI of the Brain, The University of Oxford, Oxford, United Kingdom
[4]Department of Biomedical Engineering, Vanderbilt University, Nashville, Tennessee, United States

PURPOSE. The eye and its accessory structures, the optic nerve and the extraocular muscles, form a complex dynamic system. In vivo magnetic resonance imaging (MRI) of this system in motion can have substantial benefits in understanding oculomotor functioning in health and disease, but has been restricted to date to imaging of static gazes only. The purpose of this work was to develop a technique to image the eye and its accessory visual structures in motion.

METHODS. Dynamic imaging of the eye was developed on a 3-Tesla MRI scanner, based on a golden angle radial sequence that allows freely selectable frame-rate and temporal-span image reconstructions from the same acquired data set. Retrospective image reconstructions at a chosen frame rate of 57 ms per image yielded high-quality in vivo movies of various eye motion tasks performed in the scanner. Motion analysis was performed for a left–right version task where motion paths, lengths, and strains/globe angle of the medial and lateral extraocular muscles and the optic nerves were estimated.

RESULTS. Offline image reconstructions resulted in dynamic images of bilateral visual structures of healthy adults in only ∼15-s imaging time. Qualitative and quantitative analyses of the motion enabled estimation of trajectories, lengths, and strains on the optic nerves and extraocular muscles at very high frame rates of ∼18 frames/s.

CONCLUSIONS. This work presents an MRI technique that enables high-frame-rate dynamic imaging of the eyes and orbital structures. The presented sequence has the potential to be used in furthering the understanding of oculomotor mechanics in vivo, both in health and disease.

Keywords: golden angle radial MRI, dynamic MRI, optic nerve, extraocular muscles, strabismus

The eye and orbital visual structures including the optic nerve, extraocular muscles (EOMs), and orbital fat form a highly complex dynamic system with multiple degrees of freedom. The body of work dedicated to measuring and modeling the motion of the eyes and orbital structures spans decades and includes multiple techniques.[1–9] Oculomotor measurement techniques including electro-oculograms, search coils, and infrared and video trackers provide excellent eye motion sensitivity and temporal resolution.[1] However, these techniques do not provide detailed anatomic insight on the structures of the orbit. Radiological imaging techniques, especially magnetic resonance imaging (MRI) can provide detailed anatomical information, but MRI has been used mostly in the static eye. Most biophysical models of motion of orbital structures have been based on anatomic and mechanical parameters derived from static imaging data.[2–9] Also, to our knowledge, none of these models have been fully validated with truly dynamic high-frame-rate in vivo imaging data. Therefore, a technique that combines the temporal resolution of nonimaging methods with the in vivo imaging capabilities of MRI can potentially be useful in validating and fine-tuning models of oculomotor motion.

In vivo diagnostic MRI of the eye, EOMs, and optic nerve has also mostly been restricted to static imaging with fixed gazes.[10–12] Motion is generally considered to be a confound rather than the point of interest and therefore clinical MRI is often performed under cued blinking where data are not acquired during periods of rest inserted during the scan. However, imaging of the motion of the eye, EOMs, and optic nerve can be potentially useful in understanding a range of ocular pathologies. For example, detailed analysis of patient-specific EOM motions can be potentially useful in identifying exact etiologies in complex strabismus and help in planning surgical interventions and monitoring rehabilitation.[4,13–15] In the evaluation of optic nerve gliomas, dynamic information can be helpful in determining lesion adhesions to peripheral tissue, information that is not gleaned from static MRI.[16] Knowledge of optic nerve motion can be helpful in determining altered elastic properties and strain in ocular disease. A technique to noninvasively image the dynamic moving eye, optic nerve, and EOMs can therefore add value in the clinic.

Recent advances in the field of accelerated MRI have included the development of a technique for imaging of freely moving structures with high temporal and spatial resolutions.

The method known as golden angle radial imaging has been used for several dynamic imaging applications, including imaging of the heart,[17] joints,[18] abdominal organs,[19] and even human speech,[20] but has never been applied to survey the orbit in humans. In this sequence, data are acquired continuously in a radial trajectory where the center of *k* space is sampled by each data profile. Importantly, the data profiles are spaced by a constant radial angle of 111.246°, which ensures optimal spacing between profiles and most efficient coverage of 2D *k* space.[21] For an arbitrary number of acquired profiles, a more optimal distribution of samples is generated with this sequence as compared to linearly acquired data where data profiles are stepped by 180/*P* degrees radially (*P* is usually the profile resolution, commonly 256 or 128). The main strength of this sequence, however, is the flexibility it provides in image reconstruction. In any continuously acquired radial data set (golden or linear angle), images may be reconstructed by grouping together data profiles that are acquired sequentially in time. However, in order for the images to be artifact free, the traditional linear angle radial sequence requires that the *k* space be fully sampled radially. To achieve this, *P* data profiles are necessary per reconstructed image, increasing the temporal span per image. In contrast, the unique sampling scheme of a golden angle trajectory enables artifact-free image reconstruction with significantly lower number of profiles per image, improving the temporal span per image. Furthermore, images can be reconstructed by grouping arbitrary sets of data profiles. These sets can be overlapped temporally (Fig. 1), which provides a time series of images of moving anatomy, with a freely adjustable frame rate given by $TR * p_s$, where TR is the repetition time, usually in milliseconds, and p_s is the profile step between reconstructed frames. Together, the freely adjustable image frame rate and temporal span per image lends to high-quality reconstruction of dynamic images of freely moving structures. Figure 1 gives a graphical overview of the golden angle radial sequence.

In this article, we present a proof-of-concept demonstration of the dynamic imaging of the eyes, optic nerve, and EOMs by using the above-introduced golden angle radial technique at a field strength of 3 Tesla. High-frame-rate time series in vivo MRI data are presented from volunteers performing various ocular motions in the scanner. Quantitative analyses of moving structures in the axial plane are presented as examples of potential analyses possible with motion data.

METHODS

This research followed the tenets of the Declaration of Helsinki. Participants gave written consent for participation in the study. The design of this study was approved by the Vanderbilt University Institutional Review Board (IRB). All participants were scanned after signed informed consent according to the institutional IRB.

Image Acquisition

All experiments were performed on a Philips Achieva 3 Tesla human imaging system (Philips Healthcare, Best, The Netherlands) with a 2-channel body transmit/8-channel head receive coil. Eight healthy adult subjects (31.9 ± 6.3 years of age; five male, three female) were scanned in 10 different scan sessions. Two subjects were scanned twice on different days to ensure repeatability of the imaging method. One 8-mm axial, sagittal, or coronal slice was planned on the basis of T2-weighted scout images, such that the eye globes, complete extent of the optic nerve, and the EOMs were captured in the axial, and sagittal slices (Fig. 2). Data were acquired with a golden angle (GA)
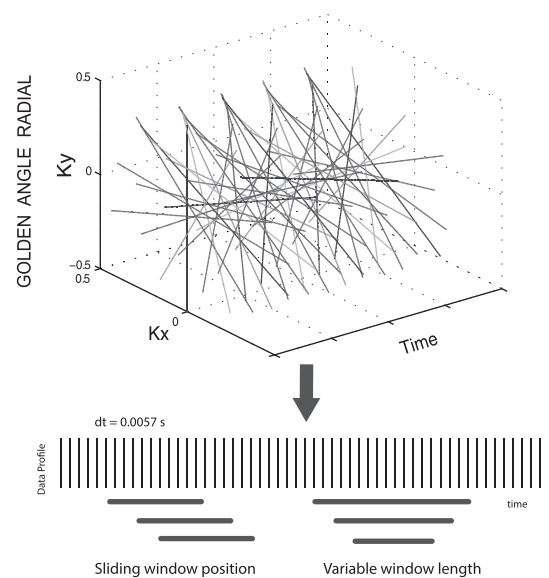

FIGURE 1. The golden angle radial imaging sequence and image reconstruction. Data profiles spaced by 111.246° are acquired continuously in time. The profiles can be grouped retrospectively to produce an image at arbitrary time positions and with arbitrary time window widths. Image can be reconstructed in a sliding window format with fast frame rates for videos of moving anatomic structures.

radial imaging sequence in which the radial spokes were stepped by 111.246° without readout alternation. Data were acquired continuously for ~15 seconds with a TR/echo time (TE) of 5.7/1.4 ms, flip angle of 20°, in-plane field of view of 200 to 224 mm (depending on the size of the head) covering both the eyes and the brain, and a readout resolution of 1 mm. A 15-second acquisition resulted in 2631 time contiguous data profiles.

To probe eye dynamics, the subjects were instructed to perform various eye movements during the scan. These included (1) resting, (2) fixating on a cross on a screen, (3) sweeping eyes from left to right and back (dextroversion/levoversion), and (4) sweeping eyes up and down (sursumversion/deorsumversion). The speed and frequency of the movements were not controlled or monitored externally. Data were acquired for only ~15 seconds per task.

Image Reconstruction

Complex time series images were reconstructed offline in Python (Anaconda version 3.4.2; Continuum Analytics, Austin, TX, USA) using 128 profiles per reconstructed image (128 × 0.0057 = 0.72-second temporal span) and a frame step of 10 radial profiles (0.057 s/frame, or ~18 frames/s). GA image reconstruction involved correction for profile *k*-space shifts and sampling density before gridding, 2D fast Fourier transform and roll-off compensation. The reconstruction steps have been presented in more detail earlier.[22] An 8-channel receive coil combination was performed in the image domain by using the method of Walsh et al.[23] to yield final dynamic images. The choice of 128 profiles per image that defined the temporal span, and profile step of 10 profiles that defined the frame rate, was arbitrary and could be adjusted freely if desired. Choices of these parameters influence the spatial and temporal quality of the dynamic images in a competing manner. To illustrate the effect of image temporal span on overall image quality, images from the fixation task were reconstructed at a chosen time point with 4, 16, 32, 64, 96, 128, 192, and 256 number of
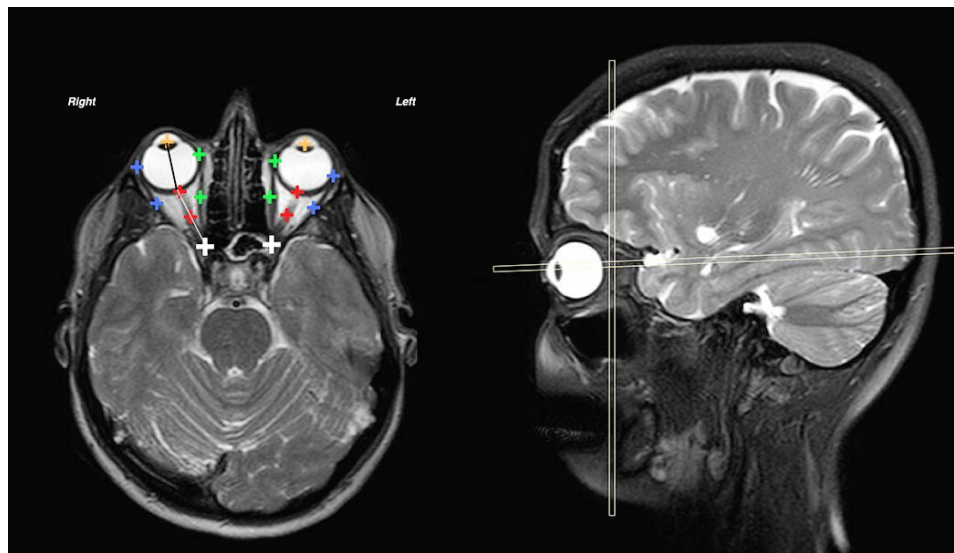
FIGURE 2. Axial and sagittal T2-weighted scout images used for planning the imaging slices. Manually landmarked points on the dynamic images for motion analysis are shown here on the axial T2w image. Lateral EOMs: *blue points*, optic nerves: *red points*, medial EOMs: *green points*, annulus of Zinn: *white points*, lens: *orange points*. EOM lengths were estimated from second-order polynomial fits to *blue* (lateral) and *green* (medial) *points*. Optic nerve lengths were estimated from fits to *red points*. The globe angle was estimated as the acute angle between the line segments joining the lens and the optic nerve head, and the optic nerve head and the AOZ (*black* and *white lines* in the right eye).

profiles, representing 0.02-, 0.09-, 0.18-, 0.36-, 0.55-, 0.72-, 1.09-, and 1.46-second time span per image frame.

Motion Analysis

An exemplary analysis of motion patterns of the eyes, optic nerve, and EOMs was performed on the levoversion/dextroversion time series image data in all subjects. Specific image landmarks that corresponded to anatomic points of interest were first identified manually in a subset of time series images 0.11 s apart (every 2 frames) and spanning 2.85 seconds (50 frames). The selected segment started with all subjects looking right, followed by sweeping the eyes to look left and sweeping the eyes to return to the original position. Fourteen points, seven per orbit, were landmarked in each time frame: the lens, the points of optic nerve junctions to the globes, the points of the extraocular muscle insertions on the globe, and one point approximately midway in each EOM and optic nerve (see Fig. 2). In addition, one common point of convergence of the optic nerve and the rectus muscles at the Annulus of Zinn (AOZ) was also marked in all images. This common landmark served as the reference in our estimation of muscle and optic nerve lengths over the version cycle.

Motion track data of the bilateral EOMs and the optic nerves were extracted by fitting the landmarked points to a second-order polynomial over the full levoversion/dextroversion cycle. A fit was performed in order to obtain a smooth approximation to the manually chosen points that naturally included some jitter. In addition to the motion tracks of the identified landmark points, the data were also used to calculate several basic parameters to better quantify the observed motions. These included the following:

1. Angles of eye movement over a version cycle: The angle of eye movement was estimated as the acute angle between the segments connecting the lens with the optic nerve head and the optic nerve head with the AOZ (Fig. 2, black and white line segments in the right eye). The angles were positive with the eyes looking left and negative when looking right.

2. Optic nerve lengths over time: The optic nerve length in each image frame was estimated by a second-order polynomial fit over three landmarked points: the optic nerve–globe junction, the midway point, and the AOZ landmark in all images for both eyes. The length of the nerve was calculated by summation of the individual fitted segments.

3. EOM lengths over a version cycle: The EOM lengths over time were estimated as the second-order fit distances from AOZ to the points of insertion of the EOM muscles on the eye globe for both eyes.

4. Strains over a version cycle: The strains induced in the EOMs and the optic nerve over the version cycle were estimated as

$$Strain = \frac{l - l_{min}}{l_{min}}$$

where l was the length of the anatomy at any time point and l_{min} was the minimum length during the version cycle. Also, the average *strain/globe angle* was estimated for all anatomic structures and subjects.

RESULTS

Dynamic time series image results for all subjects and all scans are included as movies in .mp4 format. Only segments of ~5 seconds of data are included in the Supplementary Video files owing to data file size limits. These segments, however, adequately depict the eye motions performed during these scans. These include movies of version tasks in three orientations and rest versus fixation tasks. In the text, selected frames in different orientations with time stamps are presented that cover the range of motions undertaken.

Figure 3 shows axial image frames from the rest (left column) and fixation (right column) tasks in subject 1. The entire orbital anatomy is seen with good contrast between the eye globes, optic nerve, surrounding fat, and the medial and lateral rectus muscles. Two image frames are shown, the top at an initial time of 0.36 second and the bottom at time 2 seconds. Qualitative
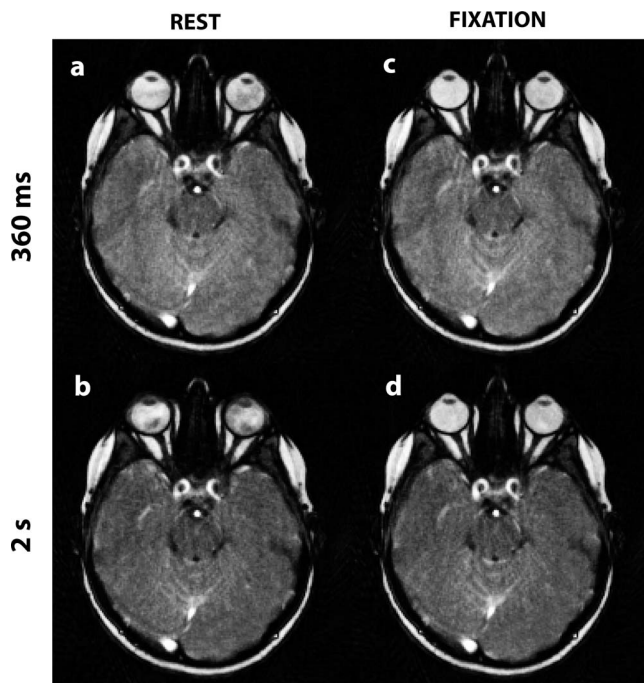
REST　　　　FIXATION

FIGURE 3. Images from subject 1 at rest and fixation at time points 360 ms and 2 seconds. Eye and optic nerve drift is observed in the rest images.

observation of the two states reveals that there is involuntary motion of the eye and optic nerve in the resting state even within 2 seconds, which is minimized by fixation. The drifting nature of this motion, especially in the right eye and optic nerve, is seen well in the video file (Supplementary Video S16, Subject 1 Scan 1 Axial Rest.mp4). Although somewhat expected, these data can help improve the design of imaging experiments, particularly where eye motion is a challenge.

Figures 4a and 4b show time frame images 0.5 seconds apart from two subjects performing left–right versions (Supplementary Video S17: Subject 1 Scan 1 Axial LR Motion.mp4; Supplementary Video S21: Subject 2 Scan 1 Axial LR Motion.mp4). Each version cycle was performed in approximately 3 seconds. Abduction/adduction of the medial/lateral rectus muscles is seen to impart large movements of the eyes along with the optic nerves. Muscle widths and the location of the muscle belly are seen to change dynamically with muscle contractions as expected. Another feature of interest is the hyperintense signal inside the globes that is seen to change with motion (see Supplementary Video file). In particular, the hyperintensity originates circumferentially at the end of each eye version and decays transiently thereafter. One hypothesis is that this signal change originates from the swirling flow of vitreous humor with highest velocities at the scleral wall, a pattern that has been predicted by some earlier modeling studies.[24-26] Similar signal change patterns were seen in all subjects. Detailed investigation of this transient signal is beyond the scope of this report. The rapid motion of the optic nerve causes some blurring in frames, especially in the middle of a version where the acceleration is highest. This is obvious, for example, in frame 5 of Figure 4a. Strategies to minimize this effect by varying the number of profiles per reconstructed image are pointed out in the discussion. Figures 4c and 4d show second-order polynomial fit motion tracks of the three landmarked points over dextroversion and levoversion, respectively, overlaid on the last frame of each version.

Figure 5 shows the results of quantitative analysis of the motion of the version cycle. The circles represent the lengths estimated from the manually selected points, and the lines represent polynomial fits to the circles. Data from all 10 scans are shown. Figures 5a and 5e, and Figures 5b and 5f show the estimated lengths of the right and left lateral and medial EOMs, respectively, over the complete version cycle (starting from looking right, then looking left, and returning to looking right). The EOM lengths are seen to vary significantly in opposing directions in the two eyes as expected. Also, the lateral and medial EOMs in each eye work in a complementary manner. Table 1 gives the estimated minimum and maximum lengths of the anatomic structures over the version cycle, averaged over the eight subjects. The medial EOM lengths were on average
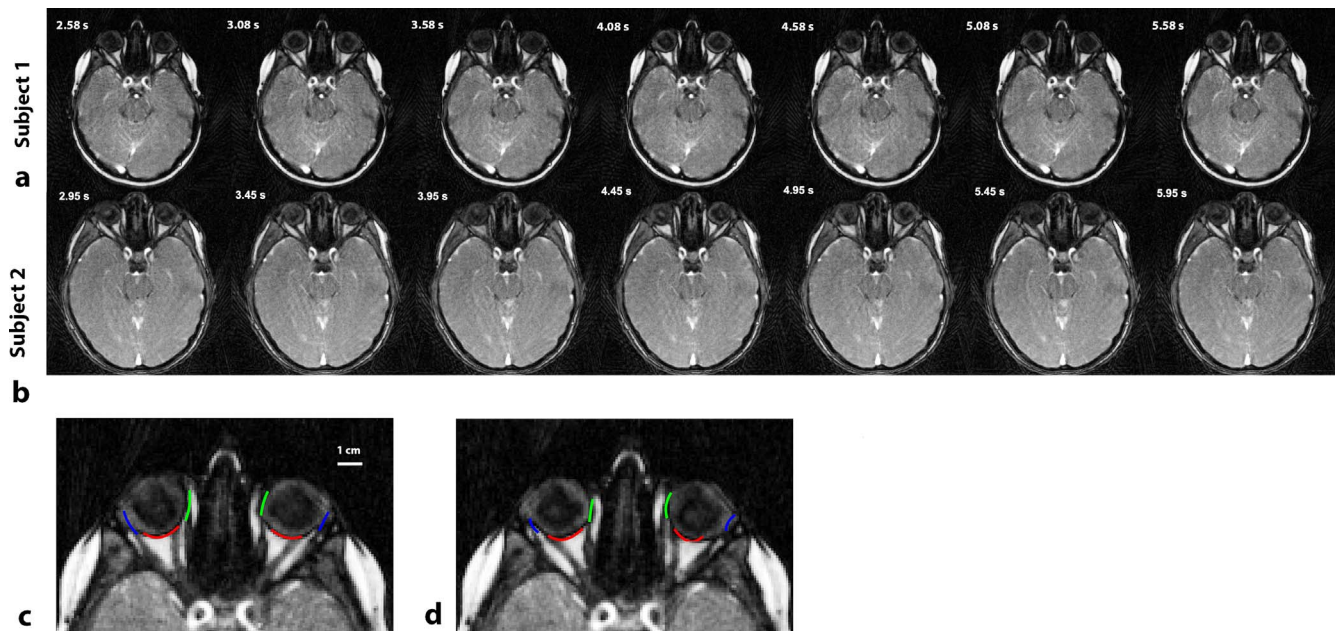

FIGURE 4. (a, b) Time frame images 0.5 s apart of left–right version task in two subjects. (c, d) Second-order polynomial fits to the landmarked point of insertion of the globes. *Blue*: lateral EOMs, *red*: optic nerves, *green*: medial EOMs. Motion tracks are displayed on top of the last frame of the dextroversion (c) and levoversion (d) task.
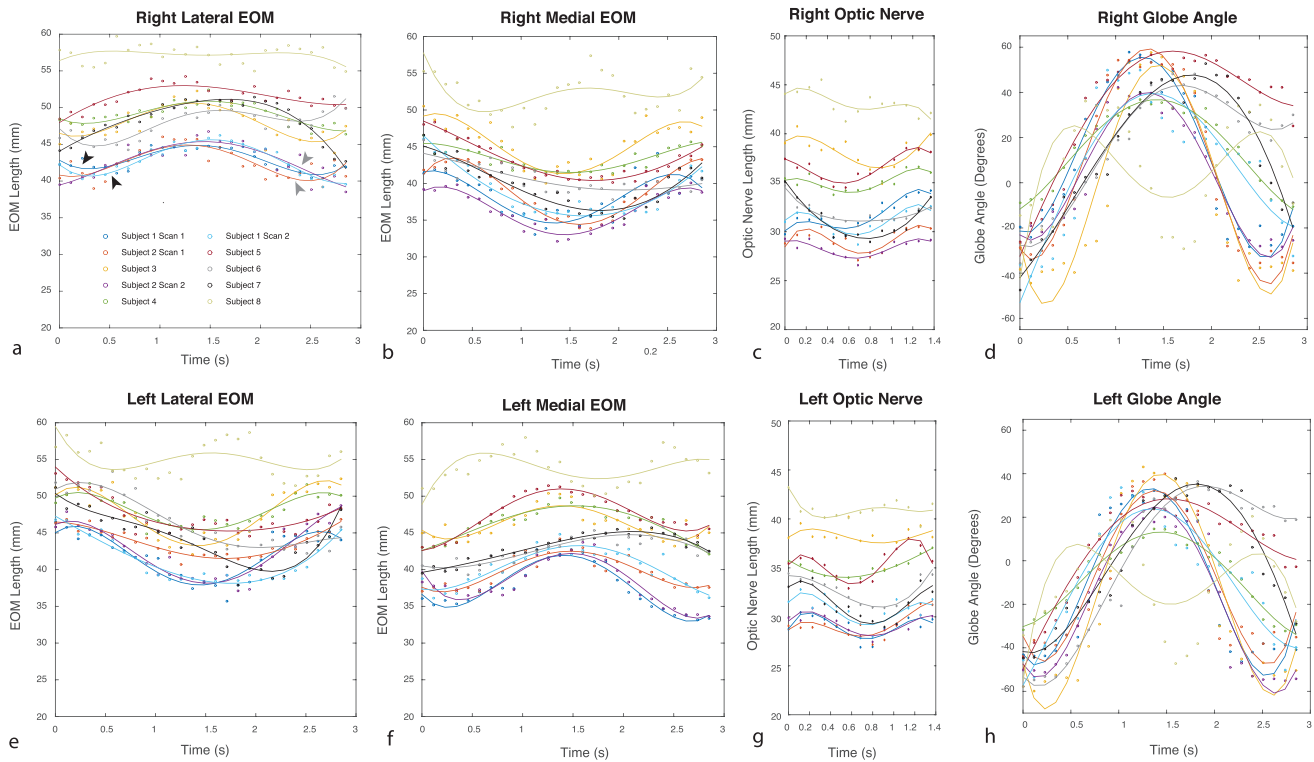
FIGURE 5. Dynamic length and angle data over the 2.85 seconds of a left–right version cycle. *Circles* represent lengths and angles estimated from manually selected points. *Solid lines* are polynomial fits to the points. Ten scans from subjects are shown. (**a**, **e**) Right and left lateral EOM lengths. *Black* and *gray arrowheads* show data from the two scans of subject 1 and subject 2, respectively. The lengths estimated from the repeated scans match closely. (**b**, **f**) Right and left medial EOM lengths. (**c**, **g**) Right and left optic nerve lengths. (**d**, **h**) Right and left globe angles.

shorter than the lateral EOMs. The black and gray arrowheads in Figure 5a show two repeated scans from two subjects. The measured lengths match closely, indicating minimal interscan variability. Figures 5c and 5g show optic nerve lengths over half of the 2.85-second period, similar in pattern to the EOM changes. Figures 5d and 5h show the globe angles during the motion. The main observation was that there is a shift in the range of angles swept by the two eye globes and a lag in the angles at any point of time. Also, in general each eye globe was seen to have a larger angle with its optic nerve when gazing in the contralateral side. Also, the variation in the optic nerve and EOM lengths follows the globe angles as expected. Since the motion was not guided by an external source, intersubject variations can be seen in the number of cycles performed

within the 2.85 seconds. Subject 10, for example, performed the task at almost double the rate of the others. The strains calculated in all the structures are shown in Supplementary Figure S1. In general larger eye rotations produce larger strains, as expected, and complementary muscles have opposite trends in strains. Table 2 shows the average *strains/degree of globe rotation* estimated over all subjects.

Figure 6 shows sagittal image frames from two subjects performing up–down versions (Supplementary Video S19: Subject 1 Scan 1 Sagittal UpDown Motion.mp4; Supplementary Video S24: Subject 2 Scan 1 Sagittal UpDown Motion.mp4). Abduction/adduction of the inferior and superior EOM is again observed, as are swirling motions of the vitreous fluid. Figure 7 (Supplementary Video S23: Subject 2 Scan 1 Coronal LR Motion.mp4; Supplementary Video S38: Subject 4 Scan 1 Coronal LR Motion.mp4) shows coronal images of left–right version movements for two subjects. The motion of the four EOMs and the optic nerve within the orbital fat are clearly observed. The inferior and superior EOMs are seen to be

TABLE 1. Average Lengths Over a Left-Right Version Cycle for Eight Subjects

Anatomy	Average Lengths Over a Left–Right Version Cycle			
	All Subjects		Without Subject 8	
	Min Length, mm	Max Length, mm	Min Length, mm	Max Length, mm
Right lateral EOM	42.4	57.2	42.4	51.4
Right medial EOM	36.5	52.2	36.5	45.4
Right optic nerve	28.3	43.2	28.3	38.0
Left lateral EOM	41.3	54.9	41.3	48.2
Left medial EOM	37.5	53.7	37.5	47.5
Left optic nerve	29.0	41.3	29.0	37.9

Max, maximum; Min, minimum.

TABLE 2. Absolute Strain/Degree of Globe Angle for All Structures Estimated Over a Left-Right Version

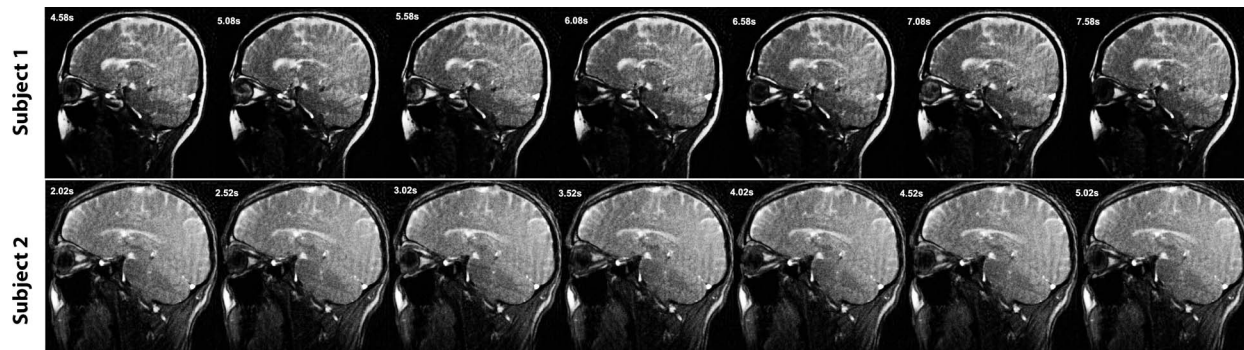|	Absolute Strain/Degree of Globe Angle, Mean ± SD
Right lateral EOM	0.00125 ± 0.0004
Right medial EOM	0.00227 ± 0.0004
Right optic nerve	0.00204 ± 0.0006
Left lateral EOM	0.00223 ± 0.0005
Left medial EOM	0.00196 ± 0.0007
Left optic nerve	0.00218 ± 0.0015

FIGURE 6. Time frame sagittal images 0.5 s apart of up–down version tasks in two subjects.

largely stationary during the left–right versions. The motion of the bilateral superior oblique muscles can also be observed.

Figure 8 shows the axial image frames reconstructed with a varying number of profiles per image to illustrate the effect of adjusting the temporal span that is uniquely allowed by the golden angle sequence. In general, the fewer the number of profiles used for reconstructing an image, the worse is the image quality, with greater streaking artifacts, low depiction of detail, and lower signal to noise ratio (SNR). While the highest detail can be seen in the image with 256 profiles per image, including fewer profiles per image might be helpful in reducing time-averaged motion effects when imaging fast-moving structures.

DISCUSSION

In this article, the proof-of-concept application of a novel in vivo MRI technique was presented that produces high-quality truly dynamic images of the bilateral orbits and the anatomic
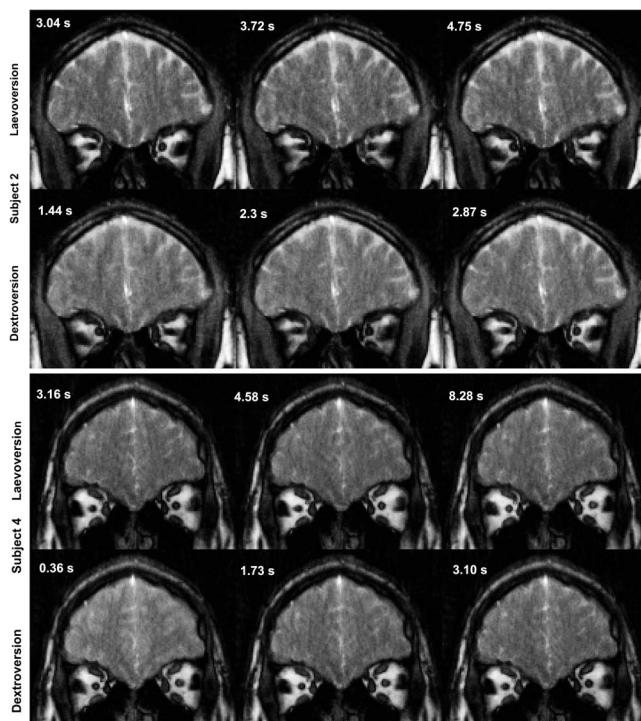

FIGURE 7. Coronal plane images of levoversion (*top*) and dextroversion (*bottom*) in two subjects. Action of all four EOMs, optic nerves, and superior oblique muscles can be observed in the motion (also see corresponding Supplementary Videos).

structures within. The primary benefit of this technique is the flexibility it offers in reconstructing dynamic images at different frame rates and time points. Successive image frames can be generated, if desired, at every repetition time (5.7 ms in this study). Therefore, data regarding positions, orientations, volumes, and strains of specific anatomic structures can be extracted at much higher sampling rates than static MRI, which typically requires at least ~100 to 200 ms per image. Therefore, not only can fast dynamic changes be captured that may be missed by static gaze imaging, but the larger number of sample points can lead to much more well-conditioned fits of parameters. Dynamic data can help better understand, for example, the time-dependent functional forms of the mechanical forces and strains in the eye and how they differ in disease. The sequence can be performed on any scanner without any external eye tracking/guidance aids and hence can be added to standard clinical MR protocols with very little additional time to yield information on patient populations. It can also be combined with non-MR techniques like optical eye tracking that can be performed inside an MR scanner. Both eyes can be imaged at the same time to extract important bilateral functional relationships during eye motion, while at the same time individual anatomic segments may be analyzed for focal diseases.

An area of clinical application of this technique could be the evaluation of strabismus, where dynamic data might aid in pinpointing the exact EOM dysfunctions involved. Patient-specific data can be used for planning surgical interventions as well as evaluation and monitoring of outcomes.[27–29] Dynamic data can aid in detecting atrophies of EOM not immediately obvious in static images. Furthermore, the imaging plane may be selected to look at any desired structure, including the superior and inferior oblique muscles.[30,31] Importantly, the golden angle sequence is very robust to bulk motion, making it an excellent candidate for pediatric MRI applications where head motion might be a challenge. This can be seen for example in subject 5 (Supplementary Video S46: Subject 5 Scan 1 Axial LR Motion.mp4) where bulk head motion is noticed along with eye motion. An additional feature is that the neurological anatomy, that is, optic chiasm and the brain, is also imaged along with the moving eye structures, creating the possibility of holistic anatomic and functional imaging. Future work will delve more deeply into characterizing the differences and testing specific hypotheses in cohorts such as different age groups and patient populations.

The main focus of this article was to introduce the application of the golden angle radial sequence to imaging the moving eye. An alternative technique that has been used before this to image the moving eye has been spin-tagging MRI.[32–34] While this method also yielded dynamic imaging data it has some limitations. First, the technique requires a long
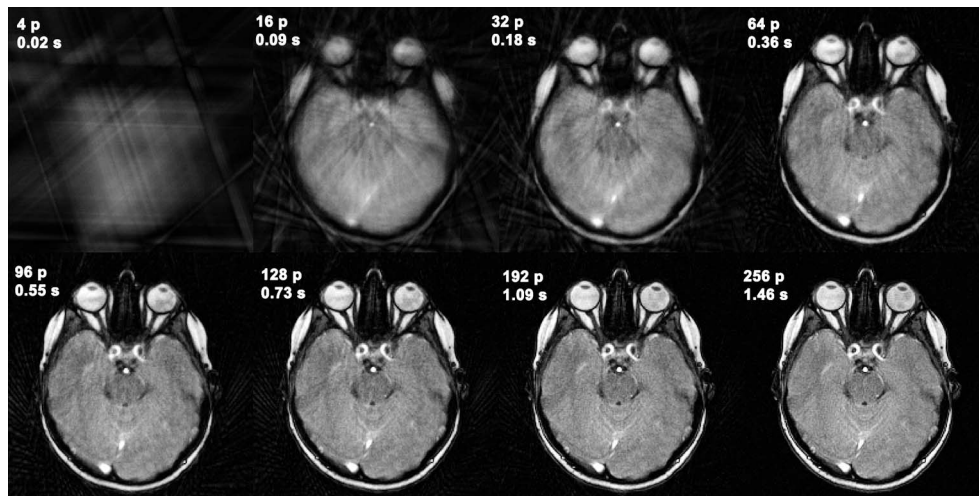
FIGURE 8. Images reconstructed from 4, 16, 32, 64, 96, 128, 192, and 256 profiles per image. Larger number of profiles improves image detail and SNR, at the cost of a larger temporal window, which can blur fast-moving structures. This flexibility of retrospective image reconstruction is provided only by the golden angle sequence.

signal recovery period relative to the actual data acquisition time. Therefore, continuous motion tracking is not possible. Multiple signal averages are generally required to get sufficient quality data. Also, the temporal resolution and the frame duration are not flexible, as in the golden angle method. The spin-tagging sequence also uses echo planar imaging, which is much more susceptible to image distortions, blurring, and other artifacts. Furthermore, the overall acquisition time is significantly higher, even for a local field of view covering one eye. Spin tagging, however, does have the benefit of allowing segmental motion analysis by following the deformation of individual tag lines. Overall, the simplicity and flexibility of the golden angle sequence might allow it to be adopted more rapidly than spin tagging.

A different fast imaging sequence commonly used in imaging moving anatomic structures is the steady-state free precession (SSFP) sequence.[35–38] SSFP gives excellent contrast between cerebrospinal fluid (CSF)-filled space, fat, and surrounding tissue. The temporal resolution that can be achieved with SSFP is high, but lower than that of the golden angle technique. In our 3-Tesla system with 80 mT/m and 200 mT/m/s maximum gradients, a singe slice $1 \times 1 \times 8$ mm^3 SSFP sequence with TR = 3.2 ms required 634 ms per image without parallel imaging, which was also the lowest possible frame rate. In contrast, the golden angle sequence provides a minimum frame rate = TR (minimum TR = ~3–3.5 ms). The golden angle method gives better contrast than SSFP in the soft tissue of the brain, but poorer CSF–nerve contrast. Also, SSFP is known to be highly vulnerable to off-resonance. Another technique used commonly to image the eye is cued blinking in which periods of rest are interleaved with fixated period of data acquisition.[39] Therefore, it is used for acquiring high-resolution, static images where cueing is used to freeze the motion that can cause artifacts in the images. The golden angle method in contrast images the eye in motion for gathering dynamic information. Therefore, the two are different techniques used to investigate different questions.

The analysis of the motion of the EOMs, optic nerve, and globes presented in this article was presented as an example of the type of quantification that can be performed with this technique. We also observed transient swirling MR signal changes inside the globes that are triggered with motion in all of our subjects. Qualitatively, these patterns look similar to the data in previous work analyzing vitreous motion using spin-

tagging MRI and vitreous flow models.[24–26,34] However, analysis of this effect is outside the scope of this article. Also, recent studies[40,41] have shown the presence of the magic angle effect in the corneoscleral shell in MRI, where fibrous microstructure of the sclera is resolved at the magic angle. We did not observe this effect in our images, likely because of the relatively low in-plane and slice resolutions ($1 \times 1 \times 8$ mm^3) of our scans causing T2* intravoxel dephasing, point spread function (PSF) broadening, as well as partial voluming.

Golden angle imaging is an area of active research in MRI, and our immediate goals are to improve its capabilities in the context of eye imaging. The first goal is to achieve improvements in the image quality and resolution to better view the structures of interest while maintaining the frame rate. Imaging is performed here over a single plane only. A near-term goal is to therefore extend this technique to 3D covering the entire orbit, with minimal compromise on image quality and temporal sampling. Recently developed stack of stars and stack of spirals with compressed sensing reconstructions might allow such fast 3D coverage with reasonable image quality.[19,20] Other non-Cartesian methods like 3D kooshball[42] and 3D Cones[42] may be used, but these methods are typically best suited for imaging isotropic fields of views. In the orbit, most of the time would be wasted in imaging structures outside the orbit, reducing the temporal efficiency. A second aim is to push the temporal resolution while maintaining modest spatial coverage. Another area of immediate effort is pushing the imaging resolution to submillimeter levels, allowing improved visualization of finer structures such as the optic nerve head and muscle pulleys in motion. We have used a slice thickness of 8 mm for our scans, which can cause partial voluming. The main influence of partial volume effect is the additional noise that is introduced when manually identifying landmarks, owing to reduced image contrast. We have used polynomial fits in our processing to be more robust to these errors. However, partial volume effects may be more of a challenge if automated image analysis methods are used to segment the anatomic structures of the orbit. A third area of development is the extension of this sequence to higher field strength, for example, 7 Tesla. Since SNR roughly scales with field strength, imaging at 7 T will provide a significant boost without a cost to imaging resolution or sampling time. Finally, most of the feature extraction in this article was manual for the sake of simplicity. The goal was to provide examples of the

types of motion analyses that may be performed on these imaging data. Future work will focus on the development of automated image analysis techniques for processing and analyses of extended time series data as well as more advanced analysis of motion.

The data in this study remain available for public use in postprocessing and modeling studies. In support of IOVS' mission of open source and reproducible research, we plan to share our source code and data with the community. The material will be freely available at https://github.com/sengup tasaikat/IOVS_Dynamic_GA_MRI_of_the_eye.

Conclusions

This work presents an MRI technique that enables high-framerate dynamic imaging of the eyes. The method is generally applicable without the need for any additional non-MRI instrumentation and allows adaptive image reconstruction for visualizing dynamic structures. The presented sequence may be potentially helpful in furthering the understanding of oculomotor mechanics both in health and disease.

References

1. Eggert T. Eye movement recordings: methods. *Dev Ophthalmol*. 2007;40:15–34.

2. Miller JM, Robinson DA. A model of the mechanics of binocular alignment. *Comput Biomed Res*. 1984;17:436–470.

3. Demer JL. Mechanics of the orbita. *Dev Ophthalmol*. 2007;40:132–157.

4. Kono R, Clark RA, Demer JL. Active pulleys: magnetic resonance imaging of rectus muscle paths in tertiary gazes. *Invest Ophthalmol Vis Sci*. 2002;43:2179–2188.

5. Schutte S, van den Bedem SP, van Keulen F, van der Helm FC, Simonsz HJ. A finite-element analysis model of orbital biomechanics. *Vision Res*. 2006;46:1724–1731.

6. Guo H, Gao Z, Chen W. Contractile force of human extraocular muscle: a theoretical analysis. *Appl Bionics Biomech*. 2016;2016:4091824.

7. Wei Q, Sueda S, Pai DK. Physically-based modeling and simulation of extraocular muscles. *Prog Biophys Mol Biol*. 2010;103:273–283.

8. Abràmoff MD, Viergever MA. Computation and visualization of three-dimensional soft tissue motion in the orbit. *IEEE Trans Med Imaging*. 2002;21:296–304.

9. Hötte GJ, Schaafsma PJ, Botha CP, Wielopolski PA, Simonsz HJ. Visualization of sliding and deformation of orbital fat during eye rotation. *Trans Vis Sci Tech*. 2016;5(4):9.

10. Fanea L, Fagan AJ. Magnetic resonance imaging techniques in ophthalmology. *Mol Vis*. 2012;18:2538–2560.

11. Townsend KA, Wollstein G, Schuman JS. Clinical application of MRI in ophthalmology. *NMR Biomed*. 2008;21:997–1002.

12. Simha A, Irodi A, David S. Magnetic resonance imaging for the ophthalmologist: a primer. *Indian J Ophthalmol*. 2012;60:301–310.

13. Demer JL, Clark RA. Magnetic resonance imaging of differential compartmental function of horizontal rectus extraocular muscles during conjugate and converged ocular adduction. *J Neurophysiol*. 2014;112:845–855.

14. Tsai T-H, Demer JL. Non-aneurysmal cranial nerve compression as cause of neuropathic strabismus: evidence from high-resolution magnetic resonance imaging. *Am J Ophthalmol*. 2011;152:1067–1073.e2.

15. Clark RA, Demer JL. Changes in extraocular muscle volume during ocular duction. *Invest Ophthalmol Vis Sci*. 2016;57:1106–1111.

16. Shofty B, Ben-Sira L, Kesler A, Constantini S. Optic pathway gliomas. *Adv Tech Stand Neurosurg*. 2015;42:123–146.

17. Feng L, Axel L, Chandarana H, Block KT, Sodickson DK, Otazo R. XD-GRASP: golden-angle radial MRI with reconstruction of extra motion-state dimensions using compressed sensing. *Magn Reson Med*. 2016;75:775–788.

18. Hopfgartner AJ, Tymofiyeva O, Ehses P, et al. Dynamic MRI of the TMJ under physical load. *Dentomaxillofac Radiol*. 2013;42:20120436.

19. Chandarana H, Feng L, Block TK, et al. Free-breathing contrast-enhanced multiphase MRI of the liver using a combination of compressed sensing, parallel imaging, and golden-angle radial sampling. *Invest Radiol*. 2013;48:10–16.

20. Lingala SG, Sutton BP, Miquel ME, et al. Recommendations for real-time speech MRI. *J Magn Reson Imaging*. 2016;43:28–44.

21. Winkelmann S, Schaeffter T, Koehler T, Eggers H, Doessel O. An optimal radial profile order based on the Golden Ratio for time-resolved MRI. *IEEE Trans Med Imaging*. 2007;26:68–76.

22. Sengupta S, Smith DS, Welch EB. Continuously moving table MRI with golden angle radial sampling. *Magn Reson Med*. 2015;74:1690–1697.

23. Walsh DO, Gmitro AF, Marcellin MW. Adaptive reconstruction of phased array MR imagery. *Magn Reson Med*. 2000;43:682–690.

24. Repetto R, Stocchino A, Cafferata C. Experimental investigation of vitreous humour motion within a human eye model. *Phys Med Biol*. 2005;50:4729–4743.

25. Repetto R, Siggers JH, Stocchino A. Mathematical model of flow in the vitreous humor induced by saccadic eye rotations: effect of geometry. *Biomech Model Mechanobiol*. 2010;9:65–76.

26. Bonfiglio A, Lagazzo A, Repetto R, Stocchino A. An experimental model of vitreous motion induced by eye rotations. *Eye Vis (Lond)*. 2015;2:10.

27. Clark RA, Demer JL. Magnetic resonance imaging of the effects of horizontal rectus extraocular muscle surgery on pulley and globe positions and stability. *Invest Ophthalmol Vis Sci*. 2006;47:188–194.

28. Wu TE, Rosenbaum AL, Demer JL. Severe strabismus after scleral buckling: multiple mechanisms revealed by high-resolution magnetic resonance imaging. *Ophthalmology*. 2005;112:327–336.

29. Coats DK, Olitsky SE. *Strabismus Surgery and Its Complications*. United States: Springer Berlin Heidelberg; 2007.

30. Suh SY, Le A, Clark RA, Demer JL. Rectus pulley displacements without abnormal oblique contractility explain strabismus in superior oblique palsy. *Ophthalmology*. 2016;123:1222–1231.

31. Suh SY, Le A, Demer JL. Size of the oblique extraocular muscles and superior oblique muscle contractility in brown syndrome. *Invest Ophthalmol Vis Sci*. 2015;56:6114–6120.

32. Piccirelli M, Luechinger R, Rutz AK, Boesiger P, Bergamin O. Extraocular muscle deformation assessed by motion-encoded MRI during eye movement in healthy subjects. *J Vis*. 2007;7(14):5.

33. Piccirelli M, Luechinger R, Sturm V, Boesiger P, Landau K, Bergamin O. Local deformation of extraocular muscles during

eye movement. *Invest Ophthalmol Vis Sci*. 2009;50:5189–5196.

34. Piccirelli M, Bergamin O, Landau K, Boesiger P, Luechinger R. Vitreous deformation during eye movement. *NMR Biomed*. 2012;25:59–66.

35. Berg I, Palmowski-Wolfe A, Schwenzer-Zimmerer K, et al. Near-real time oculodynamic MRI: a feasibility study for evaluation of diplopia in comparison with clinical testing. *Eur Radiol*. 2012;22:358–363.

36. Bieri O, Scheffler K. Fundamentals of balanced steady state free precession MRI. *J Magn Reson Imaging*. 2013;38:2–11.

37. Sheth S, Branstetter BF IV, Escott EJ. Appearance of normal cranial nerves on steady-state free precession MR images. *Radiographics*. 2009;29:1045–1055.

38. Muir ER, Duong TQ. Layer-specific functional and anatomical MRI of the retina with passband balanced SSFP. *Magn Reson Med*. 2011;66:1416–1421.

39. Berkowitz BA, McDonald C, Ito Y, Tofts PS, Latif Z, Gross J. Measuring the human retinal oxygenation response to a hyperoxic challenge using MRI: eliminating blinking artifacts and demonstrating proof of concept. *Magn Reson Med*. 2001; 46:412–416.

40. Ho LC, Sigal IA, Jan NJ, et al. Magic angle-enhanced MRI of fibrous microstructures in sclera and cornea with and without intraocular pressure loading. *Invest Ophthalmol Vis Sci*. 2014;55:5662–5672.

41. Ho LC, Sigal IA, Jan NJ, et al. Non-invasive MRI assessments of tissue microstructures and macromolecules in the eye upon biomechanical or biochemical modulation. *Sci Rep*. 2016;6: 32080.

42. Riemer F, Solanky BS, Stehning C, Clemence M, Wheeler-Kingshott CA, Golay X. Sodium ((23)Na) ultra-short echo time imaging in the human brain using a 3D-Cones trajectory. *MAGMA*. 2014;27:35–46.